



## Surface-dependent chemical equilibrium constants and capacitances for bare and 3-cyanopropyldimethylchlorosilane coated silica nanochannels

Mathias Bækbo Andersen<sup>a,\*</sup>, Jared Frey<sup>b</sup>, Sumita Pennathur<sup>b</sup>, Henrik Bruus<sup>a</sup>

<sup>a</sup> Department of Micro- and Nanotechnology, Technical University of Denmark, DTU Nanotech Building 345 East, DK-2800 Kongens Lyngby, Denmark

<sup>b</sup> Department of Mechanical Engineering, University of California, Santa Barbara, CA 93106, USA

### ARTICLE INFO

#### Article history:

Received 2 July 2010

Accepted 9 September 2010

Available online 17 September 2010

#### Keywords:

Nanofluidics

Gouy–Chapman–Stern triple-layer model

Silica nanochannels

Cyanosilane surface coating

Capillary filling

### ABSTRACT

We present a combined theoretical and experimental analysis of the solid–liquid interface of fused-silica nanofabricated channels with and without a hydrophilic 3-cyanopropyldimethylchlorosilane (cyanosilane) coating. We develop a model that relaxes the assumption that the surface parameters  $C_1$ ,  $C_2$ , and  $pK_a$  are constant and independent of surface composition. Our theoretical model consists of three parts: (i) a chemical equilibrium model of the bare or coated wall, (ii) a chemical equilibrium model of the buffered bulk electrolyte, and (iii) a self-consistent Gouy–Chapman–Stern triple-layer model of the electrochemical double layer coupling these two equilibrium models. To validate our model, we used both pH-sensitive dye-based capillary filling experiments as well as electro-osmotic current-monitoring measurements. Using our model we predict the dependence of  $\zeta$  potential, surface charge density, and capillary filling length ratio on ionic strength for different surface compositions, which can be difficult to achieve otherwise.

© 2010 Elsevier Inc. All rights reserved.

### 1. Introduction

Understanding silica surfaces is important especially in the field of micro- and nanofluidics due to the emerging applications in pharmaceuticals, environmental health and safety, and bioanalytical systems [1–3]. Additionally, silica surfaces are scientifically of great interest, displaying rich phenomena because of the coupling of surface chemistry, electrokinetics, and fluid dynamics bridging molecular and continuum macroscopic length scales. As a result, new properties are observed which are not present in the bulk, e.g. vastly increased viscosity near solid surfaces, changes in thermodynamic properties, and changes in chemical reactivity at the liquid–solid interface [4,5]. The solid–liquid interface is therefore a subject of general interest; it is here where most of the unique inherent physics of nanofluidic systems is found.

Recently, due to the advances in nanofabrication technology, there has been an increasing number of experimental studies of the solid–liquid interface using nanochannels [6–11]. Though much work has been dedicated towards understanding how the electric double layer influences the flow of electrolytes at the nanoscale [12–14], there are still large quantitative discrepancies between theoretical modeling and experimental observations [5,15]. One of the complicating factors with studying nanofluidic

transport processes is the influence from external forces typically used to drive transport at the nanoscale [2,4,5]. Therefore, capillary filling is an ideal platform to study intrinsic electrochemical reactions between the channel surface and the advancing electrolyte [9,16–18].

Janssen and co-workers [9] investigated the deprotonation in silica nanochannels during capillary filling. The authors used the pH-sensitive fluorescent dye fluorescein as an indicator of the local pH of the electrolyte in the channel during the transient capillary filling. Two regions were observed: (i) one region closest to the nanochannel entrance of full fluorescence signal and hence with the original pH (above the point of fluorescent quenching), and (ii) a dark region closest to the meniscus of no fluorescence signal and therefore with a pH equal to that of the point of zero charge  $pH_{pzc}$  of the surface (below the point of fluorescent quenching). The ratio of the extent of these two regions combined with knowledge of the composition of the buffer indicated the amount of protons that were released from the wall, which was found to be in the range 0.1–1 protons per  $nm^2$ . These values were then fitted to a theoretical model as a function of ionic strength and bulk pH, using electrolytes with different amounts of KCl and Tris–HCl buffer. Good agreement between theory and experiment was found by fitting a Stern-layer capacitance of  $2.3 F m^{-2}$ .

Although this capillary filling study has provided valuable insight regarding the solid–liquid interface of bare silica, different surface coatings have yet to be investigated, and a general theoretical model of the interface is still missing. Therefore the aim of this

\* Corresponding author. Fax: +45 45887762.

E-mail address: mathias.andersen@nanotech.dtu.dk (M.B. Andersen).

URL: <http://www.nanotech.dtu.dk/microfluidics> (M.B. Andersen).

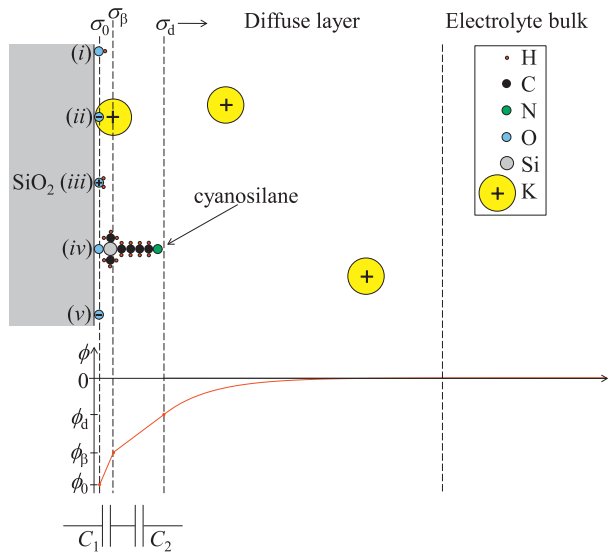


**Fig. 1.** Sketch of the solid-electrolyte interface showing the atoms/ions as hard spheres of sizes proportional to their hydrated or covalent radii (see Supporting information Sec. S2). To the left are the five possible surface site complexes: (i) SiOH, (ii) SiOK, (iii) SiOH<sub>2</sub><sup>+</sup>, (iv) SiC<sub>6</sub>H<sub>12</sub>NSi (cyanosilane), and (v) SiO<sup>-</sup>. In between the solid SiO<sub>2</sub>-wall and the charge neutral bulk there are three interfacial layers with the following surface charges:  $\sigma_0$ , the layer containing the reactive surface groups;  $\sigma_\beta$ , the layer containing adsorbed K<sup>+</sup> and cyanosilanes; and  $\sigma_d$ , the diffuse screening layer. Also indicated on the figure is a graph of the electric potential  $\phi$  (red full curve) and the three interfacial potentials  $\phi_0$ ,  $\phi_\beta$ , and  $\phi_d$ . (For interpretation of the references to colour in this figure legend, the reader is referred to the web version of this article.)

work is to extend the current model to allow surface-related parameters, such as Stern-layer capacitance  $C_s$  and the surface equilibrium  $pK_a$  constants to vary with the composition of the solid-liquid interface as sketched in Fig. 1. We quantify these dependencies combining an extended version of current theoretical modeling and capillary filling experiments in bare and coated silica nanochannels.

The paper is organized as follows: in Section 2 we present a description of our solid-liquid interface model. Next, we introduce the equations that define the model. In Section 3 we list the chemicals used in our study and present the design, fabrication, and characterization of the silica nanochannels. In Section 4 we describe the experimental setup and the experiments performed to validate our model, as well as the determination of the parameters used as input in our model. In Section 5 we show the results of our combined experimental and theoretical investigation. Finally, in Sections 6 and 7 we discuss our findings and summarize our conclusions.

## 2. Theoretical modeling

The basis of our theoretical model is the Gouy-Chapman-Stern theory [19,9] combined with the more elaborate triple-layer model [20–23] of the solid-liquid interface. This complexity of modeling is necessary to simultaneously describe the observations for bare and cyanosilane-coated silica nanochannels. Our theoretical model involves three elements: (i) chemical equilibrium of the bulk electrolyte in terms of ionic concentrations and equilibrium  $pK_a$  constants [24]; (ii) electrochemical equilibrium of the proton and metal adsorption at the surface in terms of electrostatics, concentration of adsorption sites and ions, and equilibrium  $pK_a$  constants [20,21,23]; and (iii) electrochemical coupling between bulk and surface in terms of the Poisson-Boltzmann equation. An important point in our work is that we let the surface capacitances and the

surface  $pK_a$  constants vary self-consistently with the chemical composition of the wall.

### 2.1. Schematic description of the model

We model the solid-electrolyte interface as consisting of three different interfacial layers, as sketched in Fig. 1. All quantities have been averaged on planes parallel to the silica wall, which is assumed flat on the microscopic length scale. The parameters of our model are listed in Table 1.

The first interfacial layer (subscript 0) closest to the wall consists of surface silanol sites being either neutral SiOH, deprotonated SiO<sup>-</sup>, or protonated SiOH<sub>2</sub><sup>+</sup>, which together give rise to a surface charge density  $\sigma_0$ . The electric potential here is denoted  $\phi_0$ .

The second interfacial layer (subscript  $\beta$ ) is comprised of adsorbed metallic cations, K<sup>+</sup> in this particular study. These cations produce a surface charge density  $\sigma_\beta$  at the plane defined by their mean position when adsorbed onto SiO<sup>-</sup>. The electric potential here is denoted  $\phi_\beta$ . Adsorption of anions is neglected because the bulk pH values studied in this work are always higher than  $pH_{pzc}$ .

The third interfacial layer (subscript d) is the diffuse layer of mobile ions screening the surface charge densities  $\sigma_0$  and  $\sigma_\beta$  over a distance given by the Debye-Hückel screening length  $\lambda_D$ , which in this work ranges from approximately 0.3–2 nm. When integrating the charge density of the diffuse layer along the direction perpendicular to the interface, a resulting surface charge density  $\sigma_d$

**Table 1**  
Input and output parameters used in our model.

Quantity	Symbol	Unit
<i>Input parameters, literature</i>		
Viscosity	$\eta$	Pa s
Surface tension	$\gamma$	N m <sup>-1</sup>
Relative permittivity, electrolyte	$\epsilon_r = 78$	
Ionic valences	$z$	
Chemical family	X	
Chemical family member (ion)	X <sup>z</sup>	
Valence minimum/maximum	$n_x/p_x$	
Equilibrium constants for bulk	$pK_{X,z}$	
Diffusion constants	$D$	m <sup>2</sup> s <sup>-1</sup>
Electrophoretic mobilities	$\mu$	m <sup>2</sup> s <sup>-1</sup> V <sup>-1</sup>
Total surface site density	$\Gamma_{tot}$	nm <sup>-2</sup>
$pK_-: \text{SiOH} \rightleftharpoons \text{SiO}^- + \text{H}_0^+$	$pK_-$	
$pK_K: \text{SiO}^- + \text{K}_b^+ \rightleftharpoons \text{SiOK}$	$pK_K$	
<i>Input parameters, measured</i>		
Channel dimensions	$h, w, L$	m
Contact angle	$\theta$	
Temperature	$T$	K
Fluorescent, dark zone-length	$L_{fl}, L_d$	m
Meniscus position	$L_{fl} + L_d$	m
Applied potential difference	$\Delta V$	V
Conductivity	$\sigma_{el}$	S m <sup>-1</sup>
pH of bulk	pH <sub>b</sub>	
<i>Input parameters, fitting</i>		
Inner-layer Stern capacitance	$C_1$	F m <sup>-2</sup>
Outer-layer Stern capacitance	$C_2$	F m <sup>-2</sup>
$pK_+: \text{SiOH}_2^+ \rightleftharpoons \text{SiOH} + \text{H}_0^+$	$pK_+$	
<i>Output variables, bulk</i>		
Bulk concentrations		
Molarity	$c_{X,z}$	M
Number density	$n_{X,z}$	m <sup>-3</sup>
Ionic strength	$I$	M
Debye-Hückel screening length	$\lambda_D$	m
Titration concentration of H <sup>+</sup>	$B_s$	M
<i>Output variables, surface</i>		
pH of point of zero charge	pH <sub>pzc</sub>	
Electric potentials	$\phi_0, \phi_\beta, \phi_d$	V
Surface charge densities	$\sigma_0, \sigma_\beta, \sigma_d$	C m <sup>-2</sup>
Surface site densities	$\Gamma_{\text{SiO}^-}, \Gamma_{\text{SiOH}}, \Gamma_{\text{SiOH}_2^+}, \Gamma_K$	m <sup>-2</sup>

and corresponding potential drop  $\phi_d$  are obtained. The electrical potential is defined to be zero outside the diffuse part of the double layer.

## 2.2. Bulk electrolyte chemistry

The equilibrium composition of the electrolyte is calculated using the scheme presented by Persat and co-workers [24]. This scheme builds on mass conservation, electroneutrality, and chemical equilibrium theory, and it unifies the entire system of equations for a given buffer in a systematic way that facilitates efficient numerical implementation. In our implementation of the scheme, X denotes a family of chemical species, with  $X^z$  being a particular member having valence charge  $z$ . Denoting the minimum and maximum valences within a family by  $n_X$  and  $p_X$ , respectively, the chemical equilibrium reactions for the family X are



...



where each  $pK_{X,z}$  is an equilibrium constant. For instance, for phosphoric acid the family is  $X^0 = H_3PO_4$ ,  $X^{-1} = H_2PO_4^{1-}$ ,  $X^{-2} = HPO_4^{2-}$ , and  $X^{-3} = PO_4^{3-}$  with  $p_X = 0$  and  $n_X = -3$ . In terms of ionic concentrations in the bulk, each  $pK_{X,z}$  can be expressed as

$$pK_{X,z} = -\log_{10} \left( \frac{c_{X,z} c_H}{c_{X,z+1} c_{ref}} \right), \quad (2)$$

where  $c_{X,z}$  is the concentration of species X in valence state  $z$ ,  $c_H$  is the concentration of protons, and  $c_{ref} = 1 \text{ M}$  is a reference concentration.

Mass conservation within each family implies that

$$c_X = \sum_{z=n_X}^{p_X} c_{X,z}, \quad (3)$$

where  $c_X$  equals the total analytical concentration, and electroneutrality requires

$$\sum_X \sum_{z=n_X}^{p_X} z c_{X,z} = 0. \quad (4)$$

Note that this expression is only valid outside the diffuse layer. Finally, the important auto-dissociation reaction of water is



and bases are formally modeled as deprotonation reactions, e.g. the base XOH is assigned the reaction [24]



with the  $pK_a$  assigned to be 14 to ensure that the equilibrium state is complete dissociation. The addition of a salt is modeled as the addition of the equivalent amounts of corresponding acid and base. For example, the salt  $KH_2PO_4$  is modeled as the addition of the base KOH and the acid  $H_3PO_4$ . The actual chemicals used in our experiments (see Section 3) are modeled as: (i) phosphoric acid, (ii) dihydrogen fluorescein, (iii) potassium hydroxide, and (iv) sodium hydroxide, as listed in Table 2.

From Eqs. (2)–(4) an equation for the concentration of protons  $c_H$  can be derived and solved through numerical iteration using the Matlab script developed in the group of Santiago [24]. Consequently, knowing the pH value a priori, the ionic concentrations  $c_{X,z}$  can be calculated directly. This enables us to find the bulk

**Table 2**

List of chemical families X used in this work, including formulae, valences  $z$ , equilibrium constants  $pK_{X,z}$ , diffusion constants  $D_{X,z}$ , and electrophoretic mobilities  $\mu_{X,z}$ . For  $z > 0$  and  $z < 0$  the  $pK_{X,z}$  value pertains to the reaction  $z \rightleftharpoons z - 1$  and  $z \rightleftharpoons z + 1$ , respectively.

X	Formula	$z$	$pK_{X,z}^a$	$D_{X,z}^b$ ( $10^{-9} \text{ m}^2/\text{s}$ )	$\mu_{X,z}^b$ ( $10^{-9} \text{ T}^{-1}$ )
Phosphoric acid	$H_3PO_4$	0			
		-1	2.15	0.959	-37.3
		-2	7.21	0.759	-59.1
		-3	12.33	0.824	-96.2
Fluorescein	$C_{20}H_{12}O_5$	1	2.22 <sup>c</sup>	0.57 <sup>d</sup>	22.0 <sup>d</sup>
		0			
		-1	4.34 <sup>c</sup>	0.64 <sup>e</sup>	-25.0 <sup>e</sup>
		-2	6.68 <sup>c</sup>	0.502 <sup>e</sup>	-39.5 <sup>e</sup>
Potassium hydroxide	KOH	1	14.0	1.96	76.2
		0			
Sodium hydroxide	NaOH	1	14.0	1.33	51.9
		0			
Water	$H_2O$	0		9.311 <sup>f</sup>	362.4 <sup>f</sup>
		-1	14.0	5.273 <sup>f</sup>	-205.2 <sup>f</sup>
Silanol	SiOH	1	-1.9 <sup>g</sup>		
		0			
		-1	6.8 <sup>g</sup>		
Ion pair	SiOK	0			
		-1	-0.06 <sup>g</sup>		

<sup>a</sup> For acids  $pK_a$  values are at infinite dilution and at 25 °C from Ref. [24] unless otherwise stated.

<sup>b</sup>  $D_{X,z}$  values and  $\mu_{X,z}$  values at infinite dilution at 25 °C from Ref. [25] unless otherwise stated.

<sup>c</sup>  $pK_a$  values at infinite dilution and at 25 °C from Ref. [26].

<sup>d</sup> Estimate.

<sup>e</sup>  $\mu_{X,z}$  values from Ref. [24] with  $D_{X,z}$  values calculated from these using  $D_{X,z} = \mu_{X,z} k_B T / (ze)$ .

<sup>f</sup> Here  $z = 0$  represents  $H^+$  and  $z = -1$  represents  $OH^-$ .

<sup>g</sup> For bare silica: SiOH [27,28] and SiOK [23].

concentration of protons  $B_s$  required for the titration from the initial pH in the bulk  $pH_b$  to  $pH_{pzc}$  as

$$B_s = \sum_X \sum_{z=n_X}^{p_X} z \left( c_{X,z}^{pzc} - c_{X,z}^b \right). \quad (7)$$

This quantity is necessary for relating the experimentally observed capillary filling length ratios to the model.

Finally, the bulk electrolyte is characterized by the ionic strength  $I$  and the electrical conductivity  $\sigma_{el}$ ,

$$I = \frac{1}{2} \sum_X \sum_{z=n_X}^{p_X} z^2 c_{X,z}, \quad (8a)$$

$$\sigma_{el} = e \sum_X \sum_{z=n_X}^{p_X} z \mu_{X,z} n_{X,z}, \quad (8b)$$

where  $n_{X,z} = 10^3 \text{ L m}^{-3} N_A c_{X,z}$  is the bulk ion number concentration ( $\text{m}^{-3}$ ),  $N_A$  being the Avogadro constant. Parameter values used in our model are listed in Table 2.

## 2.3. Surface chemistry

The equations for the surface chemistry involve surface reactions, surface sites, site densities, and surface equilibrium constants. Here we summarize the well established surface chemical equilibrium model involving singly coordinated surface silanol sites [29,30,20,21]



where  $SiOH_2^+$ ,  $SiOH$ , and  $SiO^-$  are the protonated, neutral, and deprotonated surface hydroxyl groups,  $H_0^+$  is a proton in solution

at the 0-plane, and  $pK_{\pm}$  the equilibrium constants, which for bare silica are  $pK_{+} = -1.9$  [27] and  $pK_{-} = 6.8 \pm 0.2$  [28]. The adsorption of cations onto negative surface hydroxyl groups can be described by a similar equilibrium reaction [30,20,21]



where  $\text{K}_{\beta}^{+}$  is the cation in solution at the  $\beta$ -plane and where  $pK_{\text{K}} = -0.06 \pm 0.30$  [23]. Note that SiOK is an ion pair, giving rise to one negative charge ( $\text{SiO}^{-}$ ) in the 0-plane and one positive charge ( $\text{K}^{+}$ ) in the  $\beta$ -plane. The point of zero charge  $\text{pH}_{\text{pzc}}$  used for the evaluation of  $B_s$  in Eq. (7) is then given as

$$\text{pH}_{\text{pzc}} = \frac{1}{2}(pK_{+} + pK_{-}). \quad (11)$$

The appearance of  $pK_{+}$  in this relation implies, together with Eq. (7), that we must keep Eq. (9a), a reaction which under normal conditions can be neglected [31]. The equilibrium equations for Eqs. (9a), (9b) and (10) are

$$pK_{+} = -\log_{10} \left( \frac{\Gamma_{\text{SiOH}} c_{\text{H},0}}{\Gamma_{\text{SiOH}_2^{+}} c_{\text{ref}}} \right), \quad (12)$$

$$pK_{-} = -\log_{10} \left( \frac{\Gamma_{\text{SiO}^{-}} c_{\text{H},0}}{\Gamma_{\text{SiOH}} c_{\text{ref}}} \right), \quad (13)$$

$$pK_{\text{K}} = -\log_{10} \left( \frac{\Gamma_{\text{K}} c_{\text{ref}}}{\Gamma_{\text{SiO}^{-}} c_{\text{K},\beta}} \right), \quad (14)$$

where  $\Gamma_{\text{SiOH}}$ ,  $\Gamma_{\text{SiOH}_2^{+}}$ , and  $\Gamma_{\text{SiO}^{-}}$  are the site densities of the neutral, positive, and negative surface silanol groups, respectively.  $\Gamma_{\text{K}}$  is the site density of ion pairs of a negative surface site and a cation, and  $c_{\text{H},0}$  and  $c_{\text{K},\beta}$  are the concentrations of protons and cations at the 0- and  $\beta$ -plane, respectively. The total available density of sites is constant, and for silica surfaces reported to be  $\Gamma_{\text{tot}} = 4.6 \times 10^{18} \text{ m}^{-2}$  [32]. In our model  $\Gamma_{\text{tot}}$  is

$$\Gamma_{\text{tot}} = \Gamma_{\text{SiOH}} + \Gamma_{\text{SiO}^{-}} + \Gamma_{\text{SiOH}_2^{+}} + \Gamma_{\text{K}}. \quad (13)$$

Silane coating is modeled by decreasing  $\Gamma_{\text{tot}}$ , see Section 5.

#### 2.4. Electrical equations and bulk/surface coupling

The bulk and surface are coupled through equations involving electrical potentials, ionic concentrations, surface charge densities, and surface capacitances. For the two inner layers the equations relating surface charge densities to site densities are

$$\sigma_0 = e(\Gamma_{\text{SiOH}_2^{+}} - \Gamma_{\text{SiO}^{-}} - \Gamma_{\text{K}}), \quad (14a)$$

$$\sigma_{\beta} = e\Gamma_{\text{K}}, \quad (14b)$$

whereas the surface charge density  $\sigma_d$  of the diffuse layer is linked to  $\phi_d$  through Grahame's equation [33]

$$\sigma_d = -\text{sgn}(\phi_d) \left[ 2\epsilon_r \epsilon_0 k_B T \sum_X \sum_{z=\pm 1}^{p_X} n_{X,z} \left( e^{-\frac{ze\phi_d}{k_B T}} - 1 \right) \right]^{\frac{1}{2}}. \quad (15)$$

Due to electroneutrality the surface charge densities are related by the constraint

$$\sigma_0 + \sigma_{\beta} + \sigma_d = 0. \quad (16)$$

Assuming charge-independent dielectric permittivities and no free charges in between the surface layers, the electric displacement field between the surface planes can be found using Gauss's law. Integrating this from the 0- to the  $\beta$ -plane and from the  $\beta$ - to the d-plane yields,

$$\phi_{\beta} - \phi_0 = -\frac{\sigma_0}{C_1}, \quad (17a)$$

$$\phi_d - \phi_{\beta} = \frac{\sigma_d}{C_2}, \quad (17b)$$

where  $C_1$  is the inner and  $C_2$  the outer layer capacitance ( $\text{F m}^{-2}$ ), which are important surface dependent parameters in our model. These capacitances are coupled in series and relate to the Stern-layer capacitance  $C_s$  as  $1/C_s = 1/C_1 + 1/C_2$ .

Using the dilute assumption to neglect higher order effects, the electrochemical potential consists of a purely entropic and a purely electric term, leading to Boltzmann distributed concentrations. The proton (cation) concentration  $c_{\text{H},0}$  ( $c_{\text{K},\beta}$ ) at the 0-plane ( $\beta$ -plane) and in the bulk  $c_{\text{H}}$  ( $c_{\text{K}}$ ) are thus related by

$$c_{\text{H},0} = c_{\text{H}} \exp \left( -\frac{e\phi_0}{k_B T} \right), \quad (18a)$$

$$c_{\text{K},\beta} = c_{\text{K}} \exp \left( -\frac{e\phi_{\beta}}{k_B T} \right). \quad (18b)$$

For use in the subsequent numerical fitting we combine Eqs. (12)–(18) to obtain

$$\Gamma_{\text{K}} = \frac{\Gamma_{\text{tot}} + \frac{\sigma_d}{e}}{1 + \frac{c_{\text{H},0}}{c_{\text{K},\beta}} \left( 10^{pK_{-}} + 2 \frac{c_{\text{ref}}}{c_{\text{H},0}} \right) 10^{pK_{\text{K}}}}, \quad (19a)$$

$$\Gamma_{\text{SiOH}} = \frac{\Gamma_{\text{tot}} + \frac{\sigma_d}{e} - \Gamma_{\text{K}}}{1 + 2 \frac{c_{\text{ref}}}{c_{\text{H},0}} 10^{-pK_{-}}}, \quad (19b)$$

$$\Gamma_{\text{SiOH}_2^{+}} = \Gamma_{\text{SiO}^{-}} - \frac{\sigma_d}{e}. \quad (19c)$$

Eqs. (1)–(19) define our model, which can be characterized as a triple layer version of the Gouy–Chapman–Stern model. A list summarizing the input and output parameters of the model is given in Table 1.

### 3. Materials and methods

#### 3.1. Chemicals

The ionic solutions used in our experiments were potassium phosphate ( $\text{KH}_2\text{PO}_4$ ) based solutions with  $pK_a = 7.21$  (Fisher Scientific P285-500). Buffer concentrations of 10, 30, 50, 100, and 383 mM were prepared by mixing  $\text{KH}_2\text{PO}_4$  powder with deionized (DI) water and titrated to the desired pH value using 1 M KOH. The fluorescent analytes used in our experiments were 0.01 mM pH-sensitive sodium fluorescein (Riedel-de Haen) and 0.01 mM pH-insensitive Alexa Fluor 488 (Invitrogen). Prior to use, bulk pH and conductivities were measured (Oakto, Inc) and all solutions were filtered using 0.2  $\mu\text{m}$  PTFE syringe filters (Nalgene). Solutions were stored at 4  $^{\circ}\text{C}$  covered by aluminum foil to prevent contamination and photo bleaching. Directly prior to experiments, buffers were heated to ambient room temperature and re-mixed with a vortexer (Dencille Scientific Inc.). These precautions ensured that both the fluorescent dye maintained constant emission properties and the solutions were well preserved.

#### 3.2. Design and fabrication of silica nanochannels

The design of the nanochannels followed that of Tas et al. [17] and Persson et al. [34]. Nanochannels were fabricated using fused-silica wafers at the UCSB nanofabrication facility with conventional MEMS processing techniques [14] based on mask design sets from DTU Nanotech [34]. The design of the channels consisted of pairwise parallel inlet/outlet microwells, each 2 mm  $\times$  5 mm rounded with 5-mm-diameter caps and etched to a depth of 1.6  $\mu\text{m}$ . The pairs of reservoir wells were connected by 12 parallel nanochannels of length  $L = 5$  cm, with etched ruler markings in increments of 100  $\mu\text{m}$ . Widths  $w$  varied from 5 to 40  $\mu\text{m}$ , with depths  $h$  on different chips of either 115, 145, or 195 nm (within  $\pm 3$  nm). Fig. 2b shows the inlet of a nanochannel during capillary filling (see Supporting information Sec. S1).

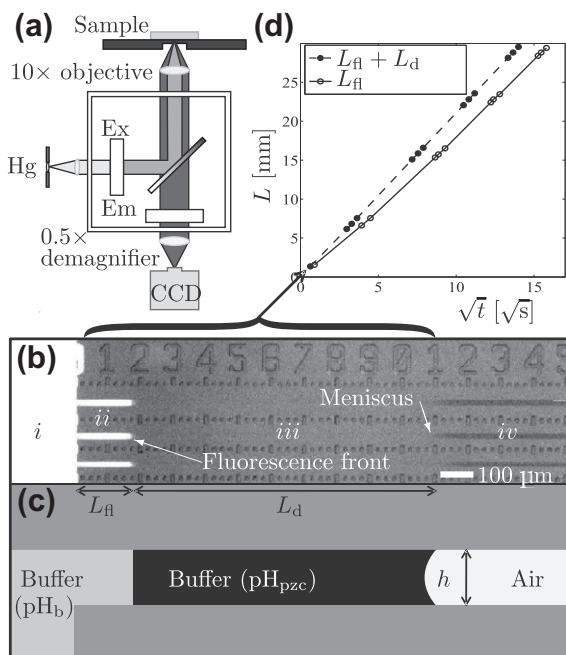


**Fig. 2.** (a) Block diagram showing the experimental setup (detailed in Section 4.1) comprising of sample, optics, mercury lamp, and EMCCD camera. (b) Image at the beginning of the capillary filling of the 30 mM  $\text{KH}_2\text{PO}_4$  buffer seeded with 0.01 mM fluorescein into three of the twelve parallel nanochannels. Four regions can be seen: (i) inlet well with fluorescent buffer, (ii) fluorescent buffer in nanochannel region of length  $L_n$ , (iii) dark buffer in nanochannel region of length  $L_d$ , (iv) black air-filled part of the nanochannel. (c) A schematic side view of one of the nanochannels of height  $h$  from panel (b) defining the lengths  $L_n$  and  $L_d$  as well as the corresponding pH conditions;  $\text{pH}_b$  in the fluorescent regions (i) and (ii), and  $\text{pH}_{\text{pzc}}$  in the dark point of zero charge region (iii). (d) Experimental capillary filling data for a bare nanochannel showing the meniscus position  $L_n + L_d$  (points and dashed line) and  $L_n$  (points and full line) versus the square root of time  $t$  (see Section 4.3). The first data point (black square) corresponds to the image in panel (b).

### 3.3. Surface coating and cleaning

To change the surface properties and characteristics of the silica nanochannels, we chose to coat the channel after fabrication with a liquid-phase silane. 3-Cyanopropyltrimethylchlorosilane (cyanosilane, Gelest Inc.) was chosen because it has been shown to form a fully wettable, slightly hydrophilic, stable lipid monolayer on glass [35], and was straightforward to coat after bonding without changing any of the channel dimensions or introducing any variability in the channel fabrication process. The coating process is known to replace  $\sim 25\%$  of negative charge sites with a neutral cyanosilane group [36] (see Fig. 1).

Immediately after fabrication and dicing, all devices were pre-cleaned using 0.2  $\mu\text{m}$ -filtered DI water driven through the nanochannels by electro-osmosis (EO). Platinum wires, inserted into the inlet/outlet microwells and fixed by scotch tape, served as EO-electrodes. The EO-flushing was powered by an electric field of 5000 V/m delivered by a source meter (Keithley 2410, sampling frequency of 100/min), and the associated electric current was monitored using a high impedance electrometer (Keithley 6517, sampling frequency of 400/min) controlled using custom LabVIEW software and analyzed with Matlab.

The initial DI-water EO-flushing ran for 60 min, while monitoring that the current remained stable at the range of  $\sim 1$  pA, after a short transient period of  $\sim 1$ –2 min. The EO-flushing was continued using 0.1 M KOH for 15 min, and finally proceeded by a second 60 min EO-flushing with DI water. At this point, the devices were either stored in DI water or treated with the cyanosilane coating.

The devices to be coated were dried on a hotplate at 150  $^\circ\text{C}$  for 30 min, after which they were filled using capillary forces with a solution of 0.1 M cyanosilane in 0.2  $\mu\text{m}$  filtered acetonitrile (Fisher Scientific). The filled nanochannels were then EO-flushed with the cyanosilane solution for approximately 30 min. The whole device was then incubated in cyanosilane solution overnight ( $\sim 12$  h) to allow the silane groups to attach themselves to the channel walls (see Supporting information Sec. S4). After this surface modification was completed, the devices were rinsed with copious amounts of filtered ethanol, EO-flushed with pure acetonitrile for 1 h, and EO-flushed with DI water for approximately 30 min until the electrical current stabilized. The coated channels were stored wet in filtered ethanol to preserve the coating and prevent degradation [37].

### 3.4. Surface characterization

The roughness of both uncoated and coated channel walls were characterized using standard AFM techniques and found to be approximately 0.3 nm and 0.7 nm, respectively (see Supporting information Sec. S1). Contact angle measurements were experimentally found by depositing 10  $\mu\text{L}$  of DI water onto each surface, and imaging the water droplets at the contact interface (see Supporting information Sec. S1). The contact angle of the uncoated and coated surfaces was found to be 32 $^\circ$  and 75 $^\circ$ , respectively, in good agreement with previously reported values [38,39]. An interferometer (Wyko NT1100) was used to image the microwell and entrance to the nanochannels (see Supporting information Sec. S1). Further characterization of the surfaces was performed using the current monitoring method, described in more detail in Section 4.2.

## 4. Experimental setup and procedure

### 4.1. Optical and electrical setup

Recordings of the propagating buffer in our filling experiments were performed using an inverted epifluorescent microscope (Olympus IX70) and automated stage (Prior Proscan II) controlled via custom LabVIEW software (LabVIEW V8.6). Images were captured using a back illuminated EMCCD camera (Andor iXon+) with a 200 ms exposure time using a 10 $\times$  objective (Olympus UPlanFL 10 $\times$  2, NA = 0.3) with a 0.5 $\times$  demagnifying lens (U-TV0.5x-C-3) as seen in Fig. 2a. A stationary halogen lamp was used to illuminate the fluid front, whereas an aligned and focused mercury arc lamp (Olympus U-RFL-T) filtered with a 488 nm excitation and 532 nm emission FITC filter cube (Chroma Technology 31001FITC/RSGFP/Fluo 3/DiO Acridine Orange(+DNA)) was used to illuminate the fluorescent front. Electric fields for channel cleaning and buffer characterization were generated across the nanofluidic channels by a Keithley multimeter (Model 2410), and currents were recorded in series with a Keithley electrometer (Model 6517) connected to platinum wire electrodes placed within each fluid reservoir of the device. A schematic of this electrical setup is shown in the inset of Fig. 3a (see Supporting information Sec. S1).

### 4.2. Current monitoring

Both the conductivity and the  $\zeta$  potential were measured by current monitoring techniques following Ref. [40]. One reservoir was initially filled with an electrolyte of concentration 0.9  $c^*$ , where  $c^*$  was a predefined target concentration. A voltage drop was applied between the inlet and outlet well to drive an EO flow. After about 15 min the current was stabilized, indicating complete filling in the nanochannel by the 0.9  $c^*$  electrolyte. Then all

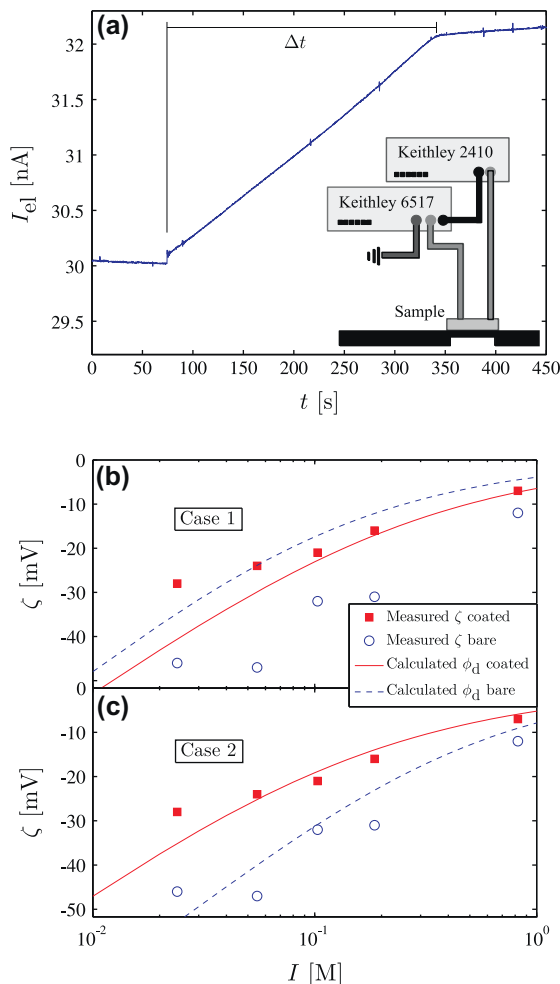


**Fig. 3.** (a) Raw data showing electrical current  $I_{el}$  versus time  $t$  in an EO-flow measurement. Initial buffer concentration is 9 mM. At  $t = 80$  s the buffer in the inlet well is replaced by a 10 mM buffer. At  $t = 340$  s the 10 mM solution has filled the channel completely. The  $\zeta$  potential is determined by Eq. (20) with  $\Delta t = 340 - 80$  s. Inset shows schematic of the experimental setup including the sourcemeter (Keithley 2410) and the electrometer (Keithley 6517), see Section 4.2. (b) Lin-log plot of measured  $\zeta$  potential for bare (blue empty circles) and coated (red filled squares) as function of ionic strength  $I$ . Curves are theoretical predictions of the diffuse layer potential  $\phi_d$  for bare (blue dashed) and coated (red full) channels for case 1, Table 5, where  $C_2 = 0.2 \text{ F m}^{-2}$ . (c) As panel (b) except that the theoretical predictions are for case 2, Table 5, where the values of  $C_2$  are  $0.8 \text{ F m}^{-2}$  and  $0.15 \text{ F m}^{-2}$  for bare and coated channels, respectively. Note the improved agreement between theory and experiment going from case 1 to case 2. (For interpretation of the references to colour in this figure legend, the reader is referred to the web version of this article.)

electrolyte was removed from the inlet well and replaced with electrolyte of concentration  $c^*$ . The current was monitored over time, with typical results shown in Fig. 3a. Measurements were performed for every concentration  $c^*$  used in the capillary filling experiments (10, 30, 50, 100, and 383 mM) at two different electric field strengths (6 kV/m and 12 kV/m). Voltage and current were supplied and monitored using the equipment described in Section 3.3. For determination of the  $\zeta$  potential, the filling speed  $L/\Delta t$  is set equal to the Helmholtz–Smoluchowski velocity ( $e\zeta/\eta)\Delta V/L$  [41],

$$\zeta = \frac{\eta L^2}{\varepsilon \Delta V \Delta t}. \quad (20)$$

Table 3, Fig. 3b and c shows measured  $\zeta$  potential for both bare and coated channels of length  $L$  at all concentrations used in this study. Also shown are theoretically fitted curves for  $\phi_d$  described in Section 5.

**Table 3**

Calculated ionic strength  $I$  from Eq. (8a), measured  $\zeta$  potential for bare and coated channels, and measured electrical conductivity  $\sigma_{el}^{meas}$  divided by  $I$ . From the fit in Fig. 4 we find  $\sigma_{el}^{meas}/I = 9.1 \text{ S m}^{-1} \text{ M}^{-1}$  in the limit  $I \rightarrow 0$ , while using Eq. (8b) in the same limit gives  $\sigma_{el}^{calc}/I = 9.36 \text{ S m}^{-1} \text{ M}^{-1}$ , deviating less than 3%.

$I$ (M)	0.024	0.055	0.103	0.186	0.823
$\zeta$ -bare (mV)	-47	-48	-32	-31	-12
$\zeta$ -coat (mV)	-29	-24	-21	-16	-7
$\sigma_{el}^{meas}/I$ ((S/m)/M)	7.083	7.909	5.728	5.000	5.033

We also characterized the electrical properties of the system by measuring the conductivity  $\sigma_{el}$  versus ionic strength  $I$ , see Table 3. This was done using both a conductivity meter and simultaneous current and voltage measurements. The Kohlrausch plot in Fig. 4 of  $\sigma_{el}/I$  versus  $I$  shows good agreement (3%) between the measured conductivity extrapolated to zero ionic strength and the theoretical dilute limit.

### 4.3. Capillary filling experiments

In our experiments, we filled both bare and cyanosilane-coated silica nanochannels with  $\text{KH}_2\text{PO}_4$  buffers of concentrations in the range 10–383 mM mixed with a 0.01 mM tracer dye, either pH-sensitive fluorescein or pH-insensitive Alexa Fluor 488 (see Section 3.1). During filling, the advancing electrolyte meniscus ( $L_n + L_d$ ) and the fluorescence front ( $L_n$ ) were recorded optically as shown in Fig. 2 using the equipment described in Section 4.1. A list of the performed experiments is given in Table 4, and the exact procedure is detailed below.

A given nanochannel was removed from its wet storage and optically examined for defects and clogs. Next we flushed the channel using EO-flow for 30 min until the current stabilized to around 1 pA, which is a typical indication that the channel is not contaminated. All the liquid was evaporated from the channel by placing the chip on a hotplate at 300 °C for 30 min before it was placed on the automated microscope stage where it was aligned and focused relative to the EMCCD camera. We then pipetted the buffer solution into the inlet microwell and recorded videos of the propagation of the meniscus using the experimental setup described in Section 4.1. To capture the entire filling process, which lasts less than 5 min, the automated stage was centered to five different positions and the filling fronts were recorded as they passed the field of view. An experimental video is provided in the Supporting information. Fig. 2d shows a typical experimental data set

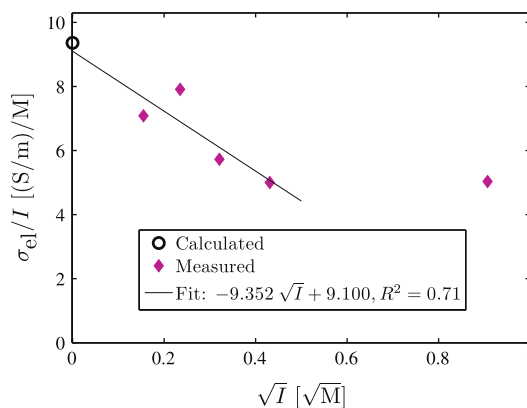


**Fig. 4.** Kohlrausch plot: the measured electrical conductivity  $\sigma_{el}$  divided by ionic strength  $I$  versus  $\sqrt{I}$ . The highest ionic strength data point clearly deviates from the Kohlrausch law and has thus been excluded from the fit. Extrapolation of the fit to  $I = 0$  deviates only 3% from the theoretically predicted value at infinite dilution (black circle), see Eq. (8b).

**Table 4**

List of the 43 capillary filling experiments, specifying the phosphate buffer concentration  $c_{\text{buf}}$  in mM, the pH of the buffer, type of the 0.01 mM dye (F: fluorescein of charge  $-2$ , A: Alexa Fluor of charge 0), type of surface (B: bare, C: cyanosilane coated), and channel height  $h$ .

#	$c_{\text{buf}}$	pH	Dye	Surf	$h$ (nm)
1–3	10	7.2	F	B	145, 145, 145
4–6	30	7.1	F	B	124, 124, 115
7–12	50	7.3	F	B	142, 142, 145, 145, 142, 142
13–19	100	7.2	F	B	145, 145, 145, 145, 142, 142, 142
20–23	383	7.2	F	B	115, 115, 115, 115
24–26	10	7.2	F	C	142, 142, 145
27–32	30	7.1	F	C	124, 124, 115, 124, 124, 115
33–35	50	7.3	F	C	142, 142, 142
36–38	100	7.2	F	C	195, 115, 115
39	383	7.2	F	C	115
40	10	7.2	A	B	142
41	100	7.2	A	B	142
42	10	7.2	A	C	115
43	100	7.2	A	C	115

demonstrating that both the fluorescent signal and the meniscus follows the Washburn relation Eq. (21). Once the channel was completely filled, we EO-flushed the channel with DI water until the current decreased to a stable level of about 1 pA. The channel was then stored wet.

#### 4.4. Extraction of parameters by capillary filling

The filling dynamics of cylindrical capillaries was first described by Washburn [42] and later applied to rectangular nanochannels of low height-to-width aspect ratio by others [17,34]. For the latter systems, relevant to this study, the time-dependent position  $L(t) = L_{\text{fl}} + L_{\text{d}}$  of the electrolyte meniscus is

$$L(t) = L_{\text{fl}} + L_{\text{d}} = \sqrt{\frac{\gamma h \cos \theta}{3\eta}} t, \quad (21)$$

where  $\gamma$  is the electrolyte/air surface tension,  $\theta$  the contact angle,  $h$  the height of the nanochannel, and  $\eta$  the viscosity of the electrolyte.

As the electrolyte containing the tracer dye fluorescein fills the nanochannel there is a region in the front of the liquid column without fluorescent signal, as shown in Fig. 2. Fluorescein is a pH-sensitive dye and therefore one might speculate that the quenching is due to a change in pH in this zone stemming from deprotonation of the silica surface silanol sites as described in Ref. [9]. This assumption is further corroborated by the fact that none of our control experiments containing pH-insensitive Alexa Fluor dye showed a region without fluorescent signal (data not shown). To evaluate the surface properties using the observed dark zone we assume that: (i) the pH is constant within each of the two regions in the liquid column, (ii) the pH in the dark region equals the value  $\text{pH}_{\text{pzc}}$  of the point of zero charge, and (iii) the pH in the fluorescent region is that of the bulk  $\text{pH}_{\text{b}}$ . With these assumptions one can estimate the amount of protons  $N_{\text{H}^+}^{\text{ads}}$  necessary to bring the volume of buffer in the dark region from  $\text{pH}_{\text{b}}$  to  $\text{pH}_{\text{pzc}}$ . This amount must equal the volume  $whL_{\text{d}}$  of the dark region multiplied by the concentration of protons  $B_{\text{s}}$  necessary to titrate from  $\text{pH}_{\text{b}}$  to  $\text{pH}_{\text{pzc}}$

$$N_{\text{H}^+}^{\text{ads}} = whL_{\text{d}}B_{\text{s}}, \quad (22)$$

where  $B_{\text{s}}$  is calculated using the theory described in Section 2.2. Note that ionic concentrations may not be constant across the nanochannel due to the influence of the electrical double layer, but for our high concentration systems the change in ionic concentration over the entire volume of the channel does not change by more than 5% from the bulk.

The release of protons from the channel walls can be estimated using the assumption that all the wall deprotonation occurs at the

interface between the dark and fluorescent regions. It then follows that by multiplying the amount per area ( $\Gamma_{\text{H}^+}$ ) of protons released by the channel wall, by the surface area in the fluorescent region of the channel, the amount of protons released into the dark region is

$$N_{\text{H}^+}^{\text{rel}} = 2(w + h)L_{\text{fl}}\Gamma_{\text{H}^+}. \quad (23)$$

Equating  $N_{\text{H}^+}^{\text{ads}}$  and  $N_{\text{H}^+}^{\text{rel}}$  yields  $\Gamma_{\text{H}^+}$  in terms of the experimentally measured lengths of the fluorescent and dark zones

$$\Gamma_{\text{H}^+} = B_{\text{s}} \frac{h}{2(1 + h/w)} \frac{L_{\text{d}}}{L_{\text{fl}}}. \quad (24)$$

Assuming that all the sites on the channel wall prior to contact with the electrolyte are SiOH, the amount of deprotonation per area is given by the surface charge density of the innermost layer as  $\Gamma_{\text{H}^+} = -\sigma_0/e$ ,  $e$  being the elementary charge. Combining this with Eq. (24) we obtain the following relation between the experimentally observed length ratio and the theoretically calculated surface charge density,

$$\frac{L_{\text{d}}}{L_{\text{fl}}} = -\frac{2(1 + h/w)}{eB_{\text{s}}h} \sigma_0. \quad (25)$$

#### 4.5. Numerical fitting procedure

We use the experimentally observed length ratios  $L_{\text{d}}/L_{\text{fl}}$  to fit  $C_1$  and  $\text{p}K_{\text{a}}$ . Below we outline the fitting procedure implemented in Matlab (see Supporting information Sec. S3) [43]. The number of independent variables is reduced to two and in the actual computation the equations are non-dimensionalized to obtain higher numerical accuracy.

1. Calculate the electrolyte ionic concentrations  $c_{\text{X},z}$  and the ionic strength  $I$  for the observed  $L_{\text{d}}/L_{\text{fl}}$ -ratio for each of the five experimental conditions  $\{c_{\text{buf}}\}_{i=1,\dots,5}$  of Table 4 using the bulk theory in Section 2.2.
2. Use the output from the bulk theory as input for the surface chemistry and bulk/surface coupling equations from Sections 2.3 and 2.4 as outlined below. Repeat until convergence.
  - (a) Estimate and update the fitting parameters  $C_1$  and  $\text{p}K_{\text{a}}$ .
  - (b) Update  $\text{pH}_{\text{pzc}}$  using Eq. (11).
  - (c) Update  $\{B_{\text{s}}\}_{i=1,\dots,5}$  from Eq. (7).
  - (d) For each  $L_{\text{d}}/L_{\text{fl}}$ -ratio give initial guess for  $\phi_0$  and  $\phi_{\text{d}}$  and solve the surface equation system:
    - i.  $\sigma_{\text{d}}$  from Eq. (15).
    - ii.  $\phi_{\beta}$  from Eq. (17b).
    - iii.  $c_{\text{H},0}$  and  $c_{\text{K},\beta}$  from Eqs. (18).
    - iv.  $\Gamma_{\text{K}}$  from Eq. (19a).
    - v.  $\sigma_{\beta}$  and  $\Gamma_{\text{SiOH}}$  from Eqs. (14b) and (19b).
    - vi.  $\sigma_0$  and  $\Gamma_{\text{SiO}^-}$  from Eqs. (16) and (13).
    - vii.  $\Gamma_{\text{SiOH}_2^+}$  from Eq. (19c).
    - viii. Check if Eqs. (12) and (17a) are converged and update  $\phi_0$  and  $\phi_{\text{d}}$  accordingly.
  - (e) Output obtained upon convergence.
  - (f) Use Eq. (25) to update the calculated length ratios  $\{L_{\text{d}}/L_{\text{fl}}\}_{i=1,\dots,5}$ . Compare these calculated length ratios against those measured. If not converged go back to 2.
3. Analyze parameters and produce goodness-of-fit values  $R^2$ , plots etc.

## 5. Results

Fig. 5 shows length ratio  $L_{\text{d}}/L_{\text{fl}}$  as function of ionic strength  $I$  measured (symbols) and fitted theoretically (curves) for bare surfaces (blue, open symbols and dashed curve) and for coated

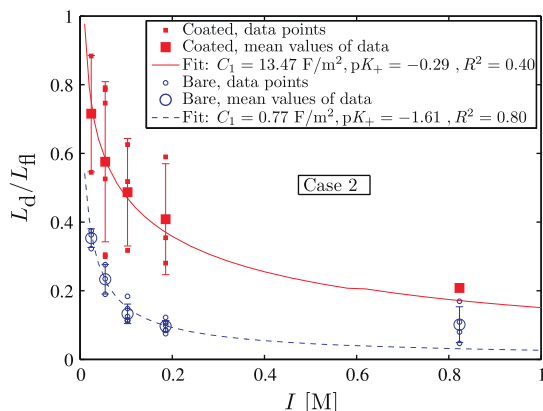


**Fig. 5.** Plot of the experimentally measured (symbols) and theoretically fitted (curves) length ratio  $L_d/L_{fi}$  as function of ionic strength  $I$  for the bare surfaces (blue, open symbols and dashed curve) and coated surfaces (red, filled symbols and full curve) with parameters corresponding to case 2 as given in Table 5. (For interpretation of the references to colour in this figure legend, the reader is referred to the web version of this article.)

surfaces (red, filled symbols and full curve). Here, the parameters kept constant are  $pK_- = 6.8$  [28] and  $pK_K = -0.06$  [23]. For the coated channels we assume that 25% of the surface sites have a cyanosilane molecule attached [36], which reduces the surface site density  $\Gamma_{tot}$  from the bare value of  $4.6 \text{ nm}^{-2}$  to  $3.45 \text{ nm}^{-2}$ . In the literature the value of  $C_2$  is often taken to be  $C_2 = 0.2 \text{ F m}^{-2}$  [23] (denoted case 1). This value of  $C_2$  did not explain the observed trends for different surfaces, and in fact, no other single fixed value could do so. We therefore allow  $C_2$  to be surface dependent. Optimization led to the values  $C_2^{\text{bare}} = 0.8 \text{ F m}^{-2}$  and  $C_2^{\text{coated}} = 0.15 \text{ F m}^{-2}$  which we denote case 2 in the following discussion. Parameters that are fitted are  $C_1$  and  $pK_+$ , and a list of parameter values for cases 1 and 2 are summarized in Table 5.

In both cases  $pK_-$ ,  $pK_K$ , and  $\Gamma_{tot}$  are parameters taken from literature [28,23,32]. In case 1, we fix the outer capacitance  $C_2$  for both the bare and coated surfaces to the value  $0.2 \text{ F m}^{-2}$  often quoted in literature [20,22,44,23]. Choosing this value of constant  $C_2$  led to fitted and calculated parameters with a decent  $R^2$  value (see Table 5) but showed poor agreement with  $\zeta$  potential experimental data. In fact, Fig. 3b shows theoretical trends which are exactly opposite of measured data, where the coated channels are estimated theoretically to have higher  $\zeta$  potential values than the bare, a trend that is not observed experimentally. In case 2 we remedy this discrepancy by optimizing  $C_2$  to not only match the  $L_d/L_{fi}$  experimental values in Fig. 5, but also the  $\zeta$  potential values in Fig. 3c. Here, we note the improved match between the calculated  $\phi_d$  and measured  $\zeta$  potential for both bare and coated data. Figs. 6 and 7 show potentials and surface charge densities for both cases. However, given the better fit of case 2 the remainder of our discussion is focused on this case.

**Table 5**

Two cases of setting the outer Stern capacitance  $C_2$ . Case 1: using the literature value  $0.20 \text{ F m}^{-2}$  for both bare (B) and coated (C) surfaces. Case 2: changing  $C_2$  to obtain match between calculated  $\phi_d$  and measured  $\zeta$ , see panel (b) and (c) in Fig. 3. Also shown are fitted and calculated parameters from Fig. 5, while other set parameters are  $pK_- = 6.8$ ,  $pK_K = -0.06$ , and  $\Gamma_{tot} = 4.6 \text{ nm}^{-2}$  (bare) and  $\Gamma_{tot} = 3.45 \text{ nm}^{-2}$  (coated).

Case	Set $C_2$ ( $\text{F/m}^2$ )	Fitted			Calculated	
		$C_1$ ( $\text{F/m}^2$ )	$pK_+$	$R^2$	$C_s$ ( $\text{F/m}^2$ )	$pH_{pzc}$
1 B	0.20	0.69	-1.03	0.81	0.16	2.9
1 C	0.20	15.47	-0.54	0.40	0.20	3.1
2 B	0.80	0.77	-1.61	0.80	0.39	2.6
2 C	0.15	13.47	-0.29	0.40	0.15	3.3

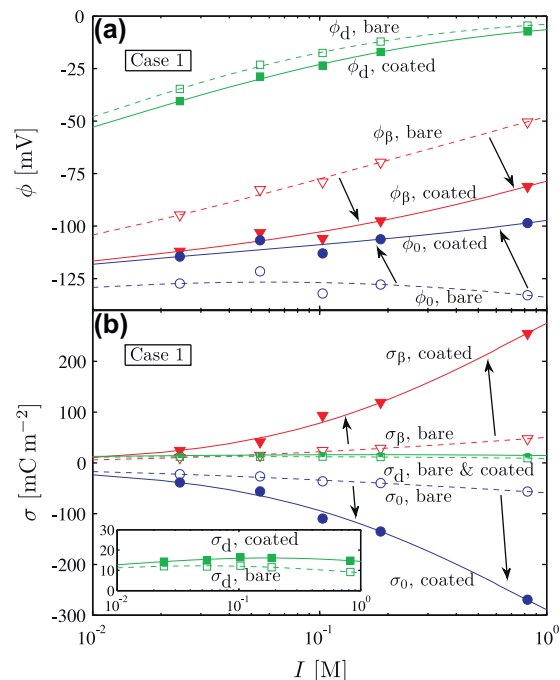


**Fig. 6.** Case 1: calculated potentials  $\phi$  and surface charge densities  $\sigma$  plotted versus ionic strength  $I$  for bare channels (open symbols and dashed curves) and coated channels (filled symbols and full curves). Each point represents the average over channel heights (see Table 4) while curves are for fixed  $h = 135 \text{ nm}$ . In this case 1  $C_2 = 0.2 \text{ F m}^{-2}$ , while other parameters are given in Table 5. (a) Calculated  $\phi_0$  (blue circles),  $\phi_\beta$  (red triangles), and  $\phi_d$  (green squares). The arrows indicate shifting of curves going from bare to coated channels. (b) Calculated  $\sigma_0$  (blue circles),  $\sigma_\beta$  (red triangles), and  $\sigma_d$  (green squares). The inset is a zoom on the diffuse layer surface charge density  $\sigma_d$ . (For interpretation of the references to colour in this figure legend, the reader is referred to the web version of this article.)

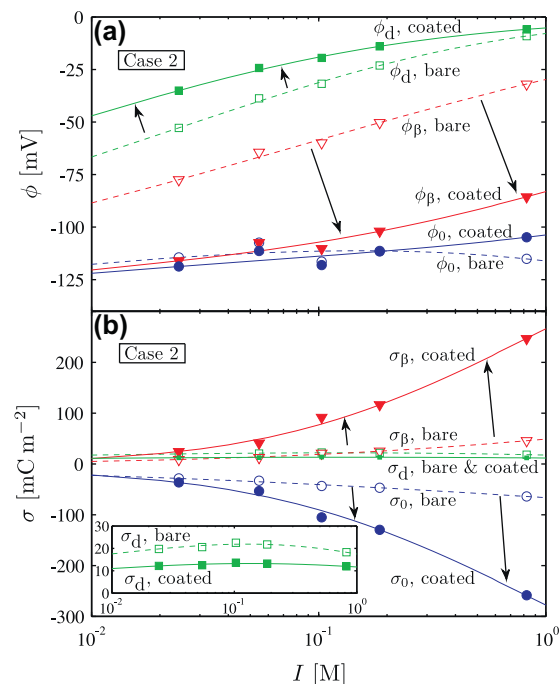


**Fig. 7.** Case 2: same as in Fig. 6 except that the parameters are:  $C_2 = 0.80 \text{ F m}^{-2}$  (bare) and  $C_2 = 0.15 \text{ F m}^{-2}$  (coated) as listed in Table 5.

Fig. 7a shows the surface potential  $\phi_0$ , the metal layer potential  $\phi_\beta$ , and the diffuse layer potential  $\phi_d$  for the bare and coated channels versus ionic strength as sketched in Fig. 1. As expected, the

values of the potentials increase from the surface layer to the metal layer to the diffuse layer. Next, we note that the metal potential  $\phi_\beta$  is much lower for coated channels than for bare channels, while the surface potential  $\phi_0$  and the diffuse potential  $\phi_d$  remain almost the same. In all cases, we note that the metal and diffuse potentials increase with ionic strength whereas the surface potential for the bare channel decreases slightly.

For cases 1 and 2, respectively, Figs. 6 and 7b show the surface charge densities at the surface, metal and diffuse layer. Here, we note that the charge density at the surface decreases with ionic strength, whereas the charge density at the metal layer increases with ionic strength, both more pronounced for the coated surface than for the bare.

By comparing Figs. 6 and 7 we note that changes in  $C_2$  primarily affect the diffuse layer potential  $\phi_d$  and charge density  $\sigma_d$ . Different values of  $C_2$  for the bare and coated surfaces will therefore not affect much the final outcome of the fitting procedure in terms of the other variables such as the surface charge density  $\sigma_0$ . This is the reason that the  $R^2$  is essentially the same for both cases as seen in Table 5. These observations speak in favor of using the values of  $C_2$  in case 2 in Table 5.

## 6. Discussion

There is a clear trend of the capillary filling length ratio  $L_d/L_\beta$  decreasing with increasing ionic strength. We can explain this through Eq. (25), where we describe the length ratio as a function of the surface charge density  $\sigma_0$  and the proton concentration  $B_s$  needed to lower the pH of the buffer front to  $\text{pH}_{\text{pzc}}$ . Since the length ratio decreases we conclude that  $B_s$  increases faster than  $\sigma_0$  decreases.  $B_s$  is mainly influenced by the  $\text{pH}_{\text{pzc}} = (\text{p}K_+ + \text{p}K_-)/2$  and thus by  $\text{p}K_+$ .

To achieve the most reliable fit with the data, we investigated the influence of  $C_1$ ,  $C_2$ ,  $\text{p}K_K$ ,  $\text{p}K_+$ ,  $\text{p}K_-$ , and  $\Gamma_{\text{tot}}$  by varying each parameter individually around some chosen reference value (see Supporting information Sec. S5). Here we summarize the observed sensitivity of each parameter. First, changing  $C_1$  raises and lowers the values of  $L_d/L_\beta$  without significantly affecting the shape of the curve. Given the fact that the bare and coated experimental data curves follow the same shape, this strongly suggests that  $C_1$  changes with surface type. Next we notice that  $C_2$ ,  $\text{p}K_K$ ,  $\text{p}K_-$ , and  $\Gamma_{\text{tot}}$  have a negligible effect on the  $L_d/L_\beta$  curve, which indicates that these parameters are most likely constant and can be determined from literature values. However, as mentioned in the previous section, we notice that varying  $C_2$  has a strong influence on the  $\zeta$  potential, which is consistent with the assumption that it only affects  $\phi_d$  and  $\sigma_d$ . Finally, we note that varying  $\text{p}K_+$  has a strong influence on the value of  $L_d/L_\beta$  at low concentrations but very little effect at high concentrations. Indeed, this is what we observe in our experimental data and therefore this suggests that  $\text{p}K_+$  must be varied with surface composition. Furthermore, because  $\text{p}K_+$  couples into  $B_s$  through  $\text{pH}_{\text{pzc}}$  it should have an influence on  $L_d/L_\beta$ . In conclusion,  $C_1$  and  $\text{p}K_+$  are our obvious choices for parameters to be fit.

The literature value of  $\text{p}K_+ = -1.9$  [27] for the bare silica surface is close to the value of  $-1.61$  theoretically determined for the bare channel when using the case 2 capacitance value of  $C_2 = 0.80 \text{ F m}^{-2}$ . For case 1 ( $C_2 = 0.20 \text{ F m}^{-2}$ ) the model calculates a higher value ( $\text{p}K_+ = -1.03$ ) which lends further support for case 2. For the coated channels  $\text{p}K_+ = -0.54$  (case 1) and  $\text{p}K_+ = -0.29$  (case 2). Given the strong evidence for case 2 parameters we believe that  $\text{p}K_+ = -0.29$  should be the value used in the future for cyanosilane-coated silica surfaces. However, we emphasize that this value is contingent upon the experimental conditions used in our study. For example, when comparing values of  $C_1$  with Wang et al. [23] we find slightly different values which most likely can be attributed to the fact that we used different electrolytes.

Examining the trends seen in Fig. 7 we note that the surface potential  $\phi_0$  varies less than 10% over the range of ionic strength used in this study, which validates a constant surface potential model in both bare and coated channels given our experimental conditions. Next, we note that the metal potential  $\phi_\beta$  and diffuse layer potential  $\phi_d$  significantly increase with increasing ionic strength, which is consistent with trends reported in literature [23]. Consistent with case 2, we hypothesize that the amount of metal ions that can adsorb onto the surface is highly dependent on the composition of the surface. Moreover, because  $C_1^{\text{bare}} \sim 0.7 \text{ F m}^{-2}$  is much lower than  $C_1^{\text{coated}} \sim 14 \text{ F m}^{-2}$  this hypothesis is further justified since  $\phi_\beta^{\text{bare}}$  is much higher than  $\phi_\beta^{\text{coated}}$ .

Finally, the surface charge density  $\sigma_0$  of the coated channels decreases more rapidly than that of the bare channels also due to the fact that  $C_1$  is much higher for the coated channels. This again indicates that more metal ions can adsorb to the surface without changing the potential. Because  $\sigma_\beta = -(\sigma_0 + \sigma_d)$ ,  $\sigma_\beta$  increases with increasing ionic strength faster in the coated channels than in the bare channels. We note that  $\sigma_d$  is relatively constant with ionic strength and surface coating providing justification to use the Grahame Eq. (15) to solve for diffuse layer potentials [30]. Using our optimized values of  $C_2$ , Fig. 3c shows that  $\sigma_d$  for the bare channel is higher than the coated channel, matching experimental trends (data not shown). We note that  $\sigma_d$  is lower than the  $60 \text{ mC m}^{-2}$  quoted in literature for fused silica nanochannels [45] but similar to the  $25 \text{ mC m}^{-2}$  quoted for amorphous silica nanochannels [46]. Stein et al. [45] used the neutral  $\text{CH}_3$  head group doctodecyltrichlorosilane as surface coating and found a decrease in the surface charge density, consistent with our curves in the inset in Fig. 7b. However, in both Refs. [45,46] aqueous KCl was used as the electrolyte in contrast to our  $\text{KH}_2\text{PO}_4$ , and as discussed in Refs. [47,48] the different co-ions may lead to different actual values of  $\sigma_d$ .

We can also use our model to examine the surface site densities  $\Gamma_i$ . Fig. 8 shows  $\Gamma_i$  for bare (open symbols and dashed curves) and coated (filled symbols and full curves) channels using case 2 parameters. The amount of adsorbed cations ( $\text{K}^+$ ) is significant for the coated channels especially at high ionic strengths when compared to the bare channels. This is consistent with the result of  $C_1$  being much higher for the coated channels than for the bare channel. Furthermore, a sensitivity analysis of the effect of  $\Gamma_{\text{tot}}$  shows that changing the amount of sites available at the wall does not change the results shown in Fig. 7 (see Supporting information Sec. S5). Therefore, our results will be relatively accurate despite

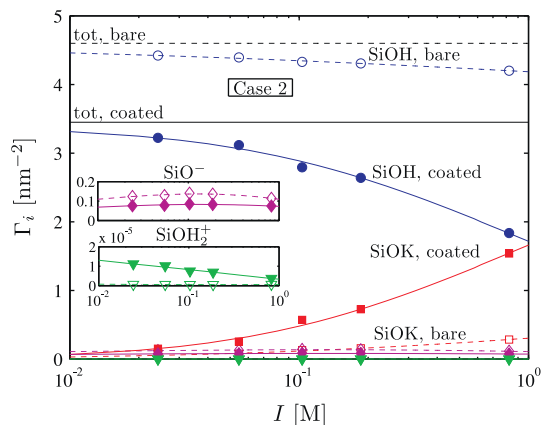


**Fig. 8.** The surface site densities  $\Gamma_i$  for bare channels (open symbols and dashed curves) and coated channels (filled symbols and full curves) for case 2. The four surface site densities are  $\Gamma_{\text{SiOH}}$  (blue circles),  $\Gamma_{\text{SiO}^-}$  (purple diamonds),  $\Gamma_{\text{SiOH}_2^+}$  (green triangles), and  $\Gamma_{\text{SiOK}}$  (red squares). The insets are magnifications of the low-density sites  $\Gamma_{\text{SiO}^-}$  and  $\Gamma_{\text{SiOH}_2^+}$ . (For interpretation of the references to colour in this figure legend, the reader is referred to the web version of this article.)

the experimental uncertainty of  $\Gamma_{\text{tot}}$  after coating with cyanosilane.

Throughout our experiments, we have assumed that the fluorescein quenches exactly at  $\text{pH}_{\text{pzc}}$ . This is a reasonable assumption as fluorescein is known to quench at pH values below 5 [49,50], and our model predicts  $\text{pH}_{\text{pzc}} < 5$  in all cases (see Table 5 and Supporting information Sec. S6).

To date, it has been difficult or almost impossible to use a model to predict experimental data mainly due to difficulties in modeling the Stern layer [15]. Here, we show that by just changing  $C_1$ ,  $C_2$ , and  $\text{p}K_+$  while using literature values for all other surface parameters, we can find  $\zeta$  potential values that almost exactly match experimentally determined values for both bare and cyanosilane-coated silica nanochannels. We believe our model will be important to predict experimentally observed phenomena, for example, geological studies have shown that silica is known to dissolve in the presence of an electrolyte [51]. This dissolution process, although negligible in microfluidic systems, may become important at the nanoscale. Therefore, having a model which can predict the change of channel size with the measured experimental values may prove to be of utility to the field. We are currently pursuing such uses of the model.

## 7. Conclusion

In this work, we presented a combined theoretical and experimental analysis of the solid–liquid interface of fused-silica nanofabricated channels with and without hydrophilic 3-Cyanopropyltrimethylchlorosilane coating. Our theoretical model couples chemical equilibrium theory of both the surface and the bulk buffer with a self-consistent extended Gouy–Chapman–Stern model of the electrochemical triple layer. We use the model to optimize the surface parameters given both experimental capillary filling data and electro-osmotic current-monitoring data, which allows for analysis of surface parameters both with and without the influence of applied external fields. Our model shows that the important fitting parameters are the capacitance  $C_1$  between the silica layer and the metal ion layer, as well as the  $\text{p}K_+$  constant. Furthermore, we find that changing the capacitance  $C_2$  between the metal ion layer and the diffuse layer with surface composition results in more accurate fits of experimentally determined  $\zeta$  potential values. This model is of value to predict experimentally observed phenomena in nanofluidic systems.

## Acknowledgments

K.G.H. Janssen is grateful acknowledged for helpful and clarifying discussions and for sharing data from Ref.[9]. We thank M.B.L. Mikkelsen and T. Wynne for help with mask design and fabrication.

## Appendix A. Supplementary material

Supplementary data associated with this article can be found, in the online version, at doi:10.1016/j.jcis.2010.09.025.

## References

- [1] T.M. Squires, S.R. Quake, *Rev. Mod. Phys.* 77 (2005) 977.

- [2] R. Schoch, J. Han, P. Renaud, *Rev. Mod. Phys.* 80 (2008) 839.  
 [3] W. Sparreboom, A. van den Berg, J.C.T. Eijkel, *Nat. Nanotechnol.* 4 (2009) 713.  
 [4] L. Bocquet, E. Charlaix, *Chem. Soc. Rev.* 39 (2010) 1073.  
 [5] M. Napoli, J.C.T. Eijkel, S. Pennathur, *Lab Chip* 10 (2010) 957.  
 [6] P.M. Biesheuvel, W.B.S. de Lint, *J. Colloid Interface Sci.* 241 (2001) 422.  
 [7] W.B.S. de Lint, P.M. Biesheuvel, H. Verweij, *J. Colloid Interface Sci.* 251 (2002) 131.  
 [8] N.R. Tas, J.W. Berenschot, P. Mela, H.V. Jansen, M. Elwenspoek, A. van den Berg, *Nano Lett.* 2 (2002) 1031.  
 [9] K.G.H. Janssen, H.T. Hoang, J. Floris, J. de Vries, N.R. Tas, J.C.T. Eijkel, T. Hankemeier, *Anal. Chem.* 80 (2008) 8095.  
 [10] H.T. Hoang, I.M. Segers-Nolten, J.W. Berenschot, M.J. de Boer, N.R. Tas, J. Haneveld, M.C. Elwenspoek, *J. Micromech. Microeng.* 19 (2009) 065017.  
 [11] R.B.H. Veenhuis, E.J. van der Wouden, J.W. van Nieuwkastele, A. van den Berg, J.C.T. Eijkel, *Lab Chip* (2009).  
 [12] C.L. Rice, R. Whitehead, *J. Phys. Chem.* 69 (1965) 4017.  
 [13] S. Pennathur, J.G. Santiago, *Anal. Chem.* 77 (2005) 6772.  
 [14] S. Pennathur, J.G. Santiago, *Anal. Chem.* 77 (2005) 6782.  
 [15] M.Z. Bazant, M.S. Kilic, B.D. Storey, A. Ajdari, *Adv. Colloid Interface Sci.* 152 (2009) 48.  
 [16] N.R. Tas, P. Mela, T. Kramer, J.W. Berenschot, A. van den Berg, *Nano Lett.* 3 (2003) 1537.  
 [17] N.R. Tas, J. Haneveld, H.V. Jansen, M. Elwenspoek, A. van den Berg, *Appl. Phys. Lett.* 85 (2004) 3274.  
 [18] L.H. Thamdrup, F. Persson, H. Bruus, A. Kristensen, H. Flyvbjerg, *Appl. Phys. Lett.* 91 (2007) 163505.  
 [19] S.H. Behrens, D.G. Grier, *J. Chem. Phys.* 115 (2001) 6716.  
 [20] J.A. Davis, R.O. James, J.O. Leckie, *J. Colloid Interface Sci.* 63 (1978) 480.  
 [21] J.A. Davis, J.O. Leckie, *J. Colloid Interface Sci.* 67 (1978) 90.  
 [22] R. Charmas, W. Piasecki, W. Rudzinski, *Langmuir* 11 (1995) 3199.  
 [23] M. Wang, A. Revil, *J. Colloid Interface Sci.* 343 (2010) 381.  
 [24] A. Persat, M.E. Suss, J.G. Santiago, *Lab Chip* 9 (2009) 2454.  
 [25] D.R. Lide, *CRC Handbook of Chemistry and Physics*, 90th ed., CRC Press/Taylor and Francis, Boca Raton, FL, 2010, (Internet Version 2010).  
 [26] S.A. Smith, W.A. Pretorius, *Water SA* 28 (2002) 395.  
 [27] T. Hiemstra, W.V. Riemsdijk, G. Bolt, *J. Colloid Interface Sci.* 133 (1989) 91.  
 [28] P. Schindler, H.R. Kamber, *Helv. Chim. Acta* 51 (1968) 1781.  
 [29] S. Levine, A.L. Smith, *Discuss. Faraday Soc.* 52 (1971) 290.  
 [30] D.E. Yates, S. Levine, T.W. Healy, *J. Chem. Soc., Faraday Trans. 1* (70) (1974) 1807.  
 [31] P.M. Biesheuvel, *J. Colloid Interface Sci.* 275 (2004) 514.  
 [32] C.G. Armistead, A.J. Tyler, F.H. Hambleton, S.A. Mitchell, J.A. Hockey, *J. Phys. Chem.* 73 (1969) 3947.  
 [33] D.C. Grahame, *Chem. Rev.* 41 (1947) 441.  
 [34] F. Persson, L.H. Thamdrup, M.B. Mikkelsen, S.E. Jaarigard, P. Skafte-Pedersen, H. Bruus, A. Kristensen, *Nanotechnology* 18 (2007) 245301.  
 [35] R.J. White, E.N. Ervin, T. Yang, X. Chen, S. Daniel, P.S. Cremer, H.S. White, *J. Am. Chem. Soc.* 129 (2007) 11766.  
 [36] S.J. Oh, S.J. Cho, C.O. Kim, J.W. Park, *Langmuir* 18 (2002) 1764.  
 [37] T. Driehorst, P. O'Neill, D.K. Fyngenson, S. Pennathur, in: *Proceedings of the Thirteenth International Conference on Miniaturized Systems on Miniaturized Chemical and BioChemical Analysis Systems (uTAS2009)*, Jeju, Korea, 1st–5th November, 2009.  
 [38] S. Falipou, J.M. Chovelon, C. Martelet, J. Margonari, D. Cathignol, *Sens. Actuators, A* 74 (1999) 81.  
 [39] S. Falipou, J. Chovelon, C. Martelet, J. Margonari, D. Cathignol, *Bioconjugate Chem.* 10 (1999) 346.  
 [40] A. Sze, D. Erickson, L. Ren, D. Li, *J. Colloid Interface Sci.* 261 (2003) 402.  
 [41] R.F. Probstein, *Physicochemical Hydrodynamics: an Introduction*, Wiley-Interscience, 1994.  
 [42] E.W. Washburn, *Phys. Rev.* 17 (1921) 273.  
 [43] The full code can be downloaded at <<http://www.nanotech.dtu.dk/microfluidics>>, 2010.  
 [44] J. Lützenkirchen, *Environ. Sci. Technol.* 32 (1998) 3149.  
 [45] D. Stein, M. Kruithof, C. Dekker, *Phys. Rev. Lett.* 93 (2004).  
 [46] R.B. Schoch, P. Renaud, *Appl. Phys. Lett.* 86 (2005) 253111.  
 [47] Y. Gushikem, J. Moreira, *J. Colloid Interface Sci.* 107 (1985) 70.  
 [48] L.T. Kubota, J.C. Moreira, Y. Gushikem, *Analyst* 114 (1989) 1385.  
 [49] M.M. Martin, L. Lindqvist, *J. Lumin.* 10 (1975) 381.  
 [50] H. Diehl, R. Markuszewski, *Talanta* 32 (1985) 159.  
 [51] G.W. Greene, K. Kristiansen, E.E. Meyer, J.R. Boles, J.N. Israelachvili, *Geochim. Cosmochim. Acta* 73 (2009) 2862.